

# Observing the vertical branch of the mesospheric circulation at latitude 60°N using ground-based measurements of CO and H<sub>2</sub>O

Peter Forkman, Patrick Eriksson, and Donal Murtagh

Onsala Space Observatory, Department of Radio and Space Science, Chalmers University of Technology, Onsala, Sweden

Patrick Espy

British Antarctic Survey, Cambridge, UK

Received 16 April 2004; revised 22 December 2004; accepted 12 January 2005; published 11 March 2005.

[1] In this report daily ground-based measurements of vertical profiles of CO and H<sub>2</sub>O from 2002 are used to trace the vertical movement of air caused by the seasonally varying mean meridional circulation. In the spring (days 100–130) the estimated ascending velocity is found to vary with time and altitude from about between 250 m/day at 65 km altitude on day 100 to a maximum of ~450 m/day at 85–90 km altitude on day 130. In the late summer and fall the descending velocity goes from 0 (when the downwelling starts) to ~250 m/day at 75 km day 280. The mesospheric adiabatic temperature changes caused by the vertical movement of air are compared to mesopause temperature as estimated by the radiance of the Meinel band OH airglow.

**Citation:** Forkman, P., P. Eriksson, D. Murtagh, and P. Espy (2005), Observing the vertical branch of the mesospheric circulation at latitude 60°N using ground-based measurements of CO and H<sub>2</sub>O, *J. Geophys. Res.*, *110*, D05107, doi:10.1029/2004JD004916.

## 1. Introduction

[2] The primary source of carbon monoxide in the mesosphere is the photolysis of carbon dioxide and the major sink is the reaction with OH. The variation of mesospheric CO is controlled by middle atmosphere dynamics since its photochemical lifetime is comparable to the time constants associated with transport processes. The dynamics of the mesosphere include planetary and gravity waves, and a seasonally varying meridional circulation, which is driven mainly by momentum flux divergences due to breaking gravity waves [e.g., Garcia *et al.*, 1992]. CO observations and model simulations have been reviewed by López-Puertas *et al.* [2000], who show that CO exhibits a strong seasonal cycle in the mesosphere and lower thermosphere, with much larger values in winter than in summer. Since CO is a good tracer of middle atmospheric dynamics; it has been used to infer the mesospheric circulation. Bevilacqua *et al.* [1985] measured CO emission at 115.27 GHz and observed large enhancements in CO column within a few days, which, after trajectory analysis, could be explained by planetary-wave activity. Aellig *et al.* [1995] made observations with a similar instrument and found variations in column density that, after comparisons with simultaneous LIDAR temperature measurements, they attributed to mixing by breaking gravity waves in the mesosphere, followed by the transport of CO-enriched air from higher altitudes. The most recent ground-based observations of middle atmospheric CO have been performed by de Zafra and Muscari [2004] and Forkman *et*

*al.* [2003b]. The Improved Stratospheric and Mesospheric Sounder (ISAMS) onboard the Upper Atmosphere Research Satellite (UARS) made the first global stratospheric/lower mesospheric CO measurements during ~6 months in 1991–1992. Allen *et al.* [2000] used ISAMS CO data to examine Antarctic polar descent in the stratosphere region.

[3] Water vapour enters the middle atmosphere primarily through the cold tropical tropopause, where most of the water vapour condenses and freezes to ice-particles. In the stratosphere the water vapour mixing ratio increases due to the oxidation of methane. At about 60 km, nearly all of the methane has been converted to water vapour, producing a water vapour volume mixing ratio peak of about 7 ppm near this altitude. Photo-dissociation due to absorption of Lyman  $\alpha$  photons results in a decreasing mixing ratio above 60 km. Transport and photo-dissociation therefore primarily determines the mixing ratio above this altitude. Since the photo-dissociation rate is reasonably well understood, measurements of the water vapour distribution above 60 km can be used to determine the timescales of mesospheric transport. Several studies have been made using ground based and satellite observations of water vapour to monitor the annual variation of the mesosphere conditions. Nedoluha *et al.* [1996] and Seele and Hartogh [1999] used ground-based measurements of the H<sub>2</sub>O emission at 22.24 GHz to discuss the annual variation of mesospheric H<sub>2</sub>O. Chandra *et al.* [1997] used data from the HALogen Occultation Experiment (HALOE) onboard UARS to examine the seasonal changes of mesospheric water vapour at low and mid latitudes.

[4] In this report daily ground based measurements of vertical profiles of CO and H<sub>2</sub>O from 2002 are used to trace the vertical movement of air. The mesospheric adiabatic

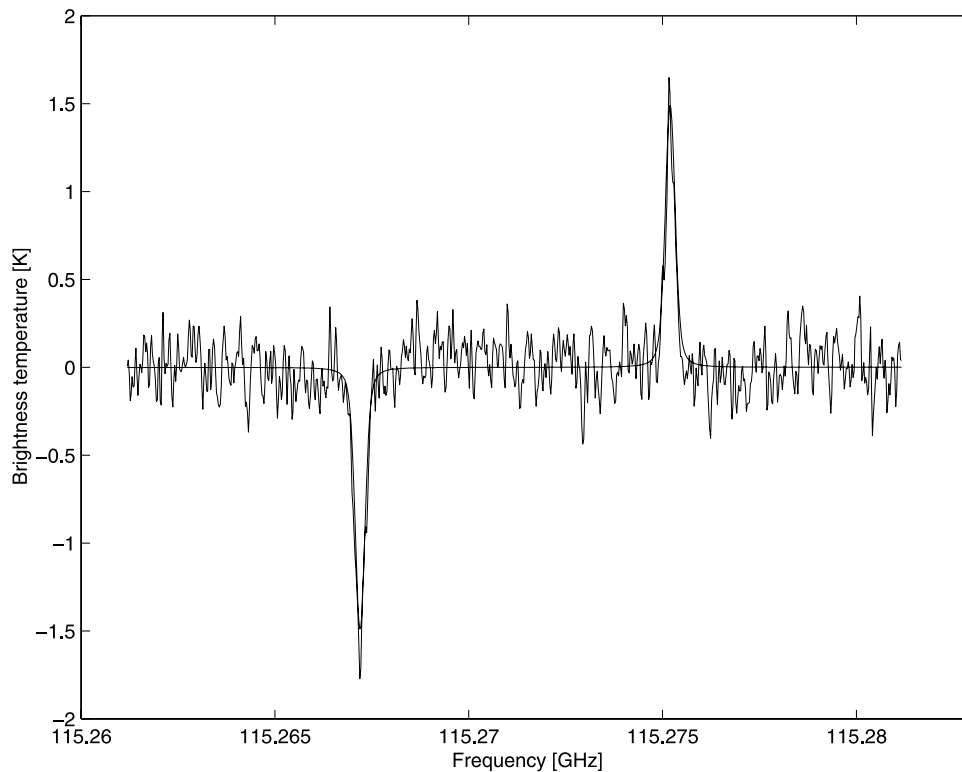


**Figure 1.** A 4-h CO spectrum corrected for the tropospheric attenuation together with a forward model fit. The channel spacing is 25 kHz. Frequency shifting is performed but in the figure only the part with the positive peak is shown.

temperature changes caused by the vertical movement of air are compared to mesopause temperature as estimated by the radiance of the Meinel band OH airglow.

## 2. Instrumentation

[5] The CO  $J = 1 \rightarrow 0$  emission at 115.271 GHz is measured with a cooled, 20 K Schottky mixer frontend system, operating in frequency-switched single sideband mode with a receiver temperature, which describes the fluctuations that the receiver adds to the measurements, of  $\sim 320$  K at a constant elevation angle of  $90^\circ$ . The H<sub>2</sub>O  $J = 6_{16} \rightarrow 5_{23}$  emission at 22.26 GHz is measured with an uncooled HEMT amplifier frontend system operating in sky-switched single sideband mode with a receiver temperature of  $\sim 250$  K. The receivers are placed at sea level at Onsala Space Observatory ( $57.4^\circ\text{N}$ ,  $12^\circ\text{E}$ ) and they share a 20-MHz, 800-delay channel autocorrelator spectrometer backend. The instruments are regularly calibrated with two known calibration loads. In-between the calibration measurements the variation of the receiver noise temperature is assumed to be less than 5% (checked by several calibration campaigns), which is a sufficient assumption to determine the brightness temperatures of the atmosphere. This simplification together with a contribution from an incorrect compensation for the tropospheric attenuation, gives a total estimated calibration error of 5%. The instruments and the measurement techniques are described in Forkman [2003] and Forkman *et al.* [2003a, 2003b].

[6] The radiance of the OH airglow is measured using a compact Michelson interferometer with an indium–

gallium–arsenide (InGaAs) detector, and the spectral region between 1000 and 1700 nm is scanned at a resolution of 0.5 nm. The instrument observes the zenith sky through an infrared-glass port in the roof of the observatory. The instrument and the measuring technique are described by Espy *et al.* [1987].

## 3. Observations

[7] Figure 1 shows a four-hour CO spectrum taken on 12 May 2002 and Figure 2 shows a three-day spectrum of H<sub>2</sub>O taken on 4–6 April 2002. In addition to the frequency and temperature-dependent Doppler broadening (full width half maximum is  $\sim 60$  kHz, for H<sub>2</sub>O and  $\sim 200$  kHz for CO) air pressure also affects the observed transition and therefore the measured shape of the line profile contains information on the abundance of the emitting constituent as a function of pressure (or height respectively). The difference between CO and H<sub>2</sub>O regarding their residence region is clearly seen in Figures 1 and 2. Large volume mixing ratios of CO at high altitudes (low pressure) gives the CO line profile its typical Gaussian line shape since the broadening mechanism is dominated by Doppler shift caused by thermal motion. H<sub>2</sub>O, on the other hand, has its peak middle atmospheric mixing ratios at lower altitudes and the H<sub>2</sub>O line profile is therefore dominated by the pressure broadening giving the observed Lorentz line shape. Using this technique for measuring vertical profiles the temperature broadening gives the upper limit and the width of the used spectrometer gives the lower limit of the vertical range. The vertical profile of the species, of course, also affects the

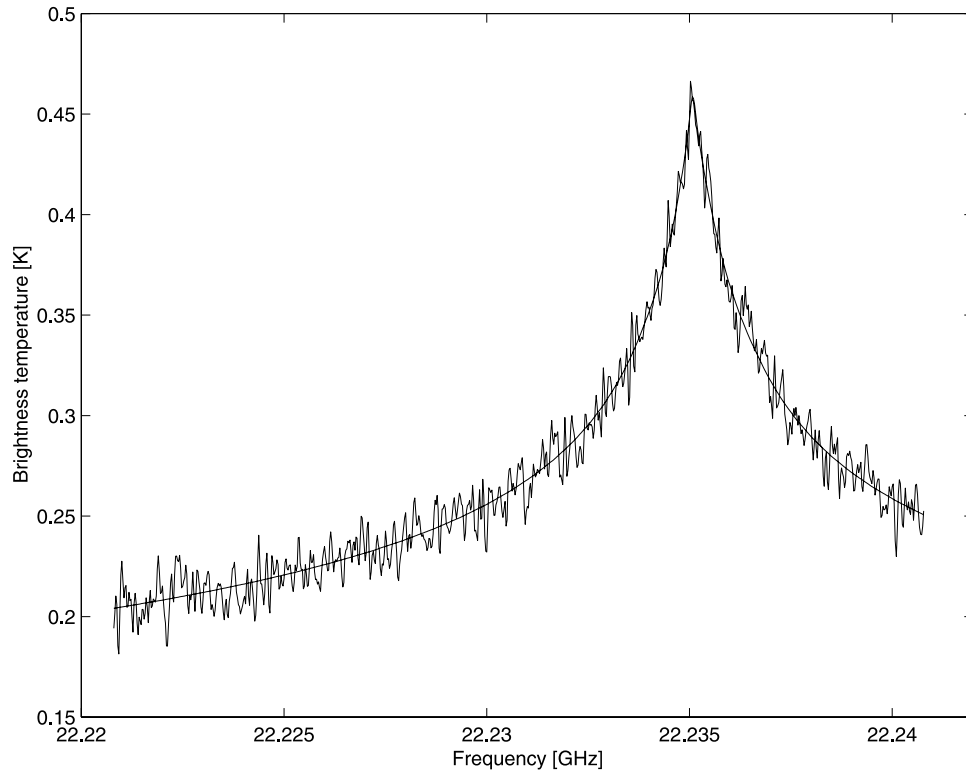
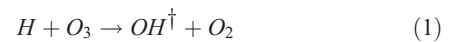


**Figure 2.** A 3-day H<sub>2</sub>O spectrum corrected for the tropospheric attenuation together with a forward model fit. The channel spacing is 25 kHz.

measurement response at the different altitudes. The vertical resolution is limited by the spectrometer resolution and the observation geometry. At ground-based measurements emission from all altitudes contributes to the spectra at all frequencies (since we always look through the complete atmosphere) and since we use a high spectrometer resolution (25 kHz) the limit of the vertical resolution is dominated by the up-looking observation technique. The thermal emission at microwave wavelengths depends only linearly on the temperature. Therefore, normally, model monthly means are used as the temperature profile. Another benefit by using microwave frequencies is that the LTE assumption can be used up to  $\sim 100$  km altitude. Vertical profiles have been calculated from the averaged spectra using a package based on the optimal estimation method [Eriksson, 2000]. Figures 3 and 4 summarize the measurements, during 2002, of CO and H<sub>2</sub>O respectively. The optimal estimation method combines information from the measurement with a priori information on the vertical profile to be retrieved. In the figures only results where the result is dominated by the measurement (high measurement response) is presented. All vertical profiles are retrieved at the same pressure grid. The seasonally varying vertical movement of this pressure grid, due to the varying temperature profile, is clearly seen in the figures (especially in Figure 4 where the upward and downward movements of the isobars are about 2 km at  $\sim 60$  km altitude). Apart from the meandering pressure levels the varying advection through the isobars is clearly seen in both figures with upward motion in the spring and downward motion in the fall.

[8] At night, the OH radical is produced naturally in the upper mesosphere in a relatively thin,  $\sim 8$  km thick layer,

and at a nearly constant altitude of  $\sim 87$  km. The responsible chemical reactions are given below:



The OH formation chemistry produces a strong chemiluminescence of the near infrared, the vibration–rotation Meinel bands, which may be observed at night from the ground. Due to the large mass differential in the OH molecule, the rotational structure of these bands extends over a large wavelength range and may be easily resolved in the spectrum. Since these rotational levels are in local thermodynamic equilibrium over the narrow altitude range of the OH, the distribution of radiance within the rotational structure may be used to remotely sense the temperature of the neutral atmosphere near the peak of the OH layer. Hence, ground-based spectroscopic studies of the OH nightglow have been used extensively to infer the atmospheric temperature near 87 km. A time series of temperature measured from Stockholm (59.4°N, 18°E) 1991–1998 is presented in Figure 5. The temperature data show a strong,  $\sim 60$  K, annual variation with the lowest temperatures in the summer.

#### 4. Data Analysis

[9] Since the chemical lifetimes for CO, in the complete mesosphere, and for H<sub>2</sub>O in the lower mesosphere, is on the

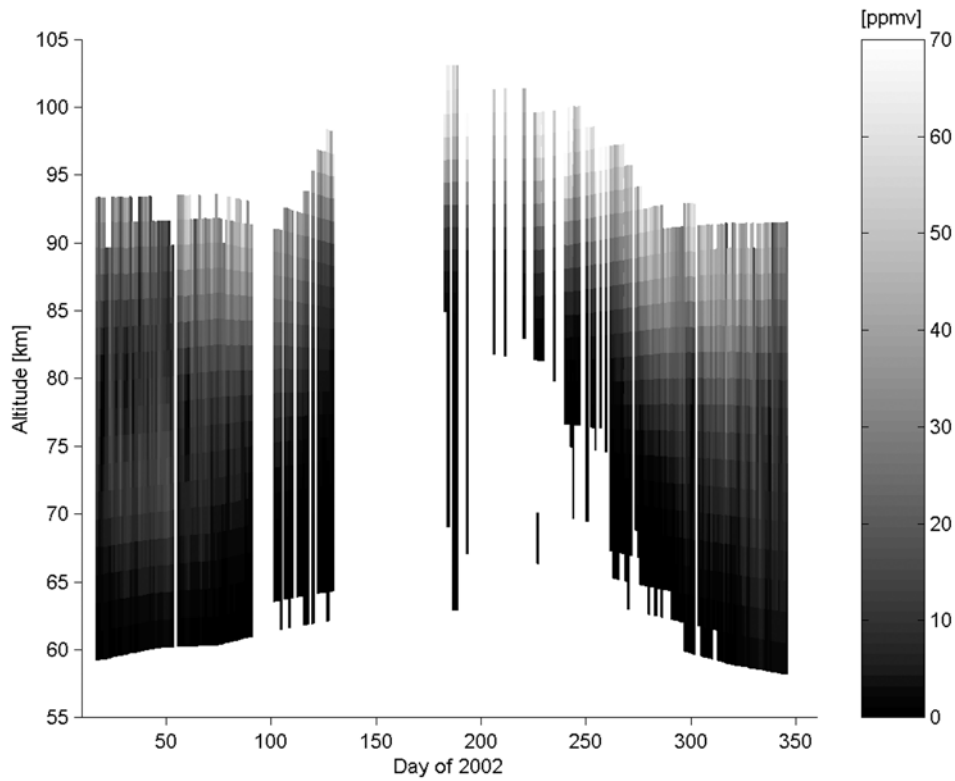


**Figure 3.** Volume-mixing ratios of CO as a function of day of 2002 and altitude is shown. See color version of this figure in the HTML.

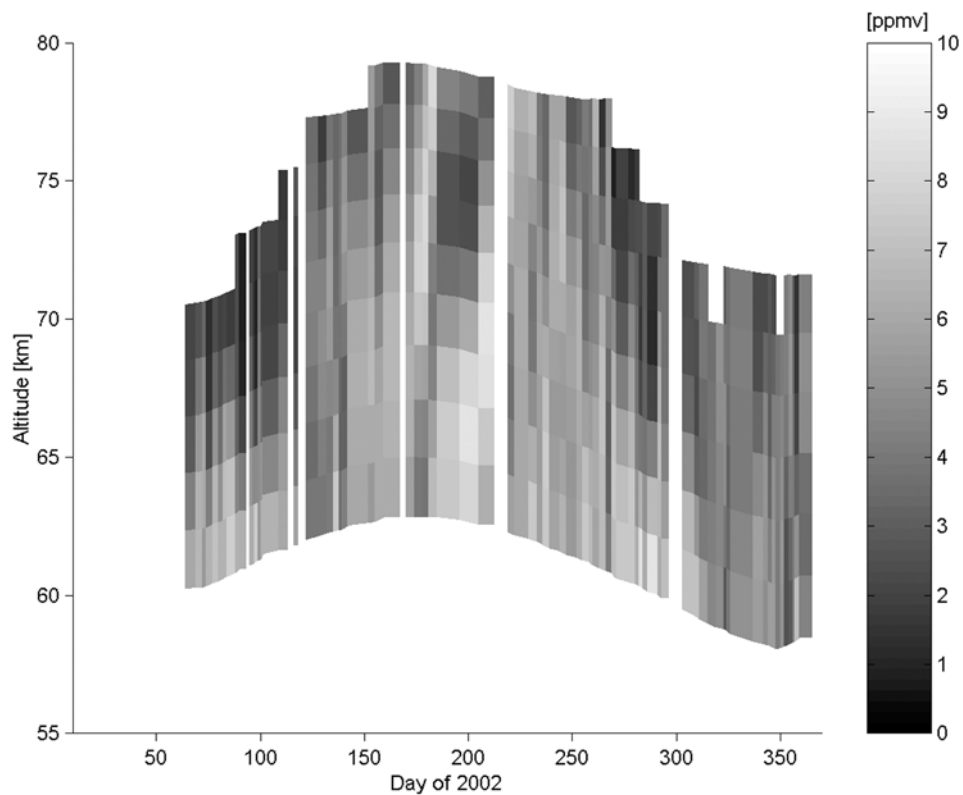


**Figure 4.** Volume-mixing ratios of H<sub>2</sub>O as a function of day of 2002 and altitude is shown. The low mixing ratios between 70 and 75 km around day 200 can be explained by observation errors due to the very bad weather these days. See color version of this figure in the HTML.

## Hydroxyl Meinel (3,1) Rotational Temperatures, Stockholm, Sweden

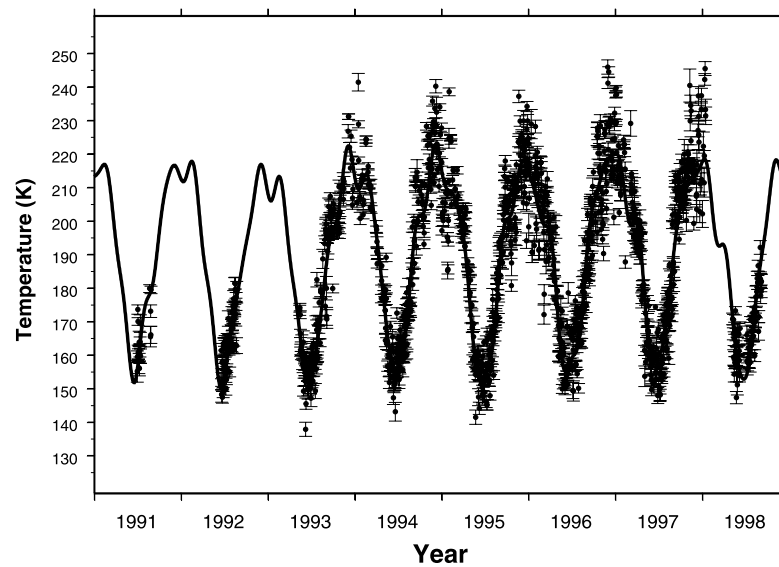


**Figure 5.** Hydroxyl Meinel (3,1) band rotational temperature nightly averages in K. The result of a least square fit to the average, trend and periodic components, described by *Espy and Stegman* [2002], are shown by the smooth curve.

order of months monitoring of these molecules can be used to trace dynamics of weeks-months duration in these respectively regions. The air at different altitudes is characterized by its volume-mixing ratio of CO or H<sub>2</sub>O respectively and since these different ratios are assumed to be constant during a month the vertical velocity of air can be estimated.

#### 4.1. CO Data Processing

[10] Figure 6 shows a typical vertical CO profile from the inversion process, where the volume-mixing ratio increases with altitude as explained in section 1, and in Figure 3 the vertical movement of CO isopleths (air with a constant CO volume-mixing ratio) is shown. The mesospheric dynamical cycle is clearly seen with both the summer scenery with upwelling air in the spring and downwelling air in the autumn and the winter scenery, which is characterized with a high variability due to wave driven horizontal movement. In this study we focus on the upwelling branch between days 100 and 130 and the downwelling branch between days 210 and 300.

[11] From day to day with measurements we monitor the movement of 12 different isopleths (constant volume mixing ratios) namely the 1, 2, 3, 4, 6, 10, 15, 20, 25, 30, 35 and 40 ppm levels. A polynomial of the second degree is fitted for each used isopleths in Figure 6 for time periods day 100–130 and day 210–300 individually. From the slope of these polynomial fits the vertical velocity of each isopleth and day can be calculated (see Figure 7).

[12] The errors in the altitude estimation of the isopleths can be described as the standard deviation between the data points and the polynomial fit. These errors for the 12 different isopleths and the two periods of time are shown in Figure 8. In this figure typical altitude errors due to the thermal noise in the measurements are also shown. This altitude error is calculated from vertical profiles like in

Figure 6 where the observation errors are included. The deviations from the polynomial fit seem to be explained by thermal noise in the springtime episode but in the autumnal episode a combination of thermal noise and atmospheric variability is needed to explain the deviation from the fit.

[13] If the vertical velocity, within each time period, is defined as the mean altitude change divided by half the time period, the error in the estimated velocity,  $dv$ , can be written

$$dv = \frac{2}{N\sqrt{N}} \cdot \frac{dh}{dt} \quad (3)$$

where  $dh$  is the altitude error and  $N$  is the number of data points used in the polynomial fit. Figure 9 shows errors in the vertical velocities for the different isopleths and time periods.

#### 4.2. H<sub>2</sub>O Data Processing

[14] As in the case of CO measurements we monitor the movement of different isopleths namely the 3.5, 4.5, 5.5 and 6.5 ppm volume-mixing ratio levels. Figure 10 shows a typical vertical H<sub>2</sub>O profile from the inversion process, where the volume-mixing ratio decreases with altitude in the mesosphere as explained in section 1, and in Figure 4 the vertical movement of H<sub>2</sub>O isopleths (air with a constant H<sub>2</sub>O volume-mixing ratio) is shown.

[15] The altitude movement and vertical speeds are calculated in the same way as in the CO data processing. The vertical velocities are seen in Figure 7. And as described for the CO measurements the errors in the estimated velocities can also be calculated and they are in the order of 30 m/day (~10 %). The discrepancy between the CO and H<sub>2</sub>O data sets can be explained by the fact the estimated velocity errors are higher for both low CO mixing ratios, which are found in the low range

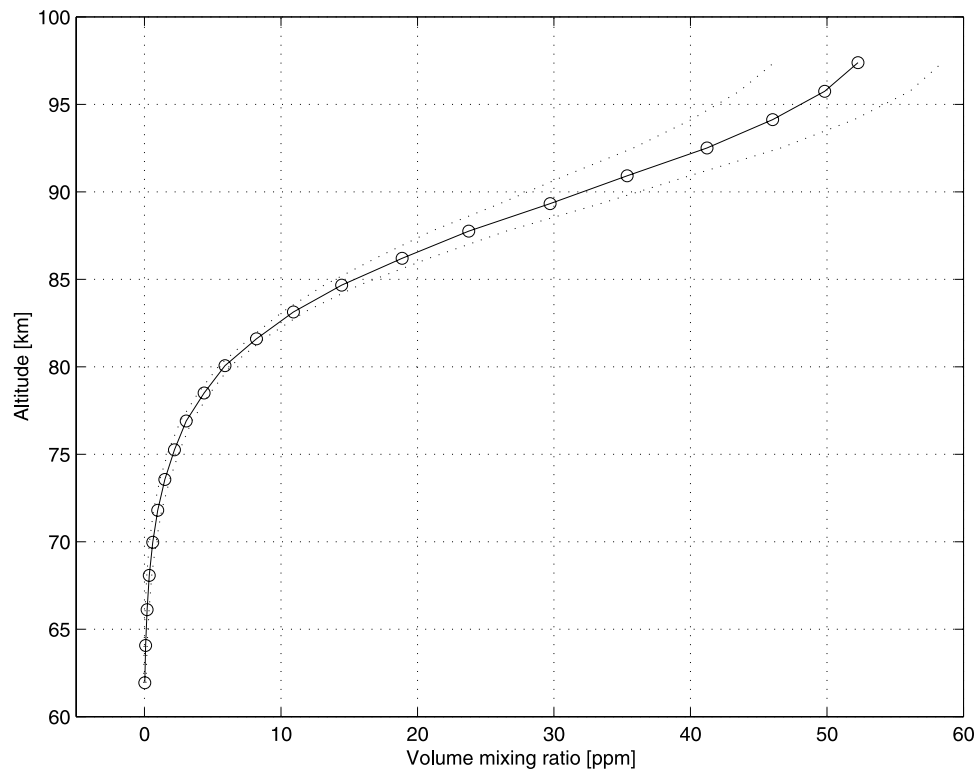


**Figure 6.** CO profile from the middle of Mars 2002. Dots with circles show the retrieved results. The solid line shows linear interpolated values and the dashed line shows the  $1\sigma$  error estimation from the noise in the measurements.

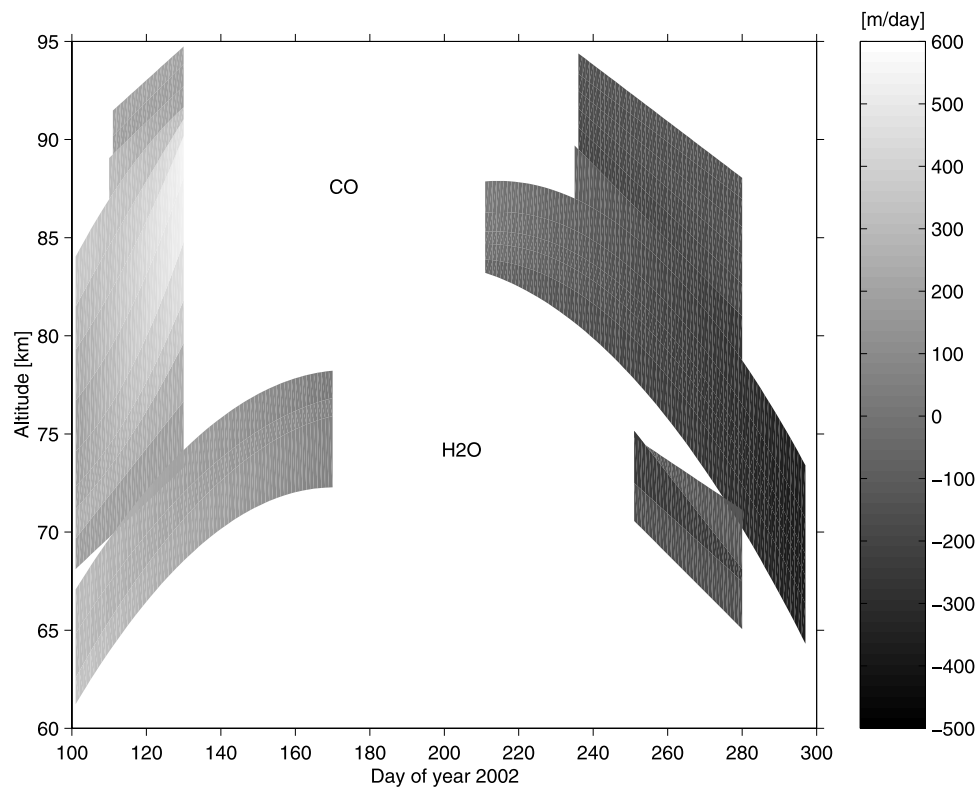


**Figure 7.** Vertical velocities of CO and H<sub>2</sub>O as a function of day and altitude. Each isopleth is seen as a contour stripe. The different shapes of these contour stripes are explained by the fact that different polynomial degrees are used (1:st or 2:nd). See color version of this figure in the HTML.

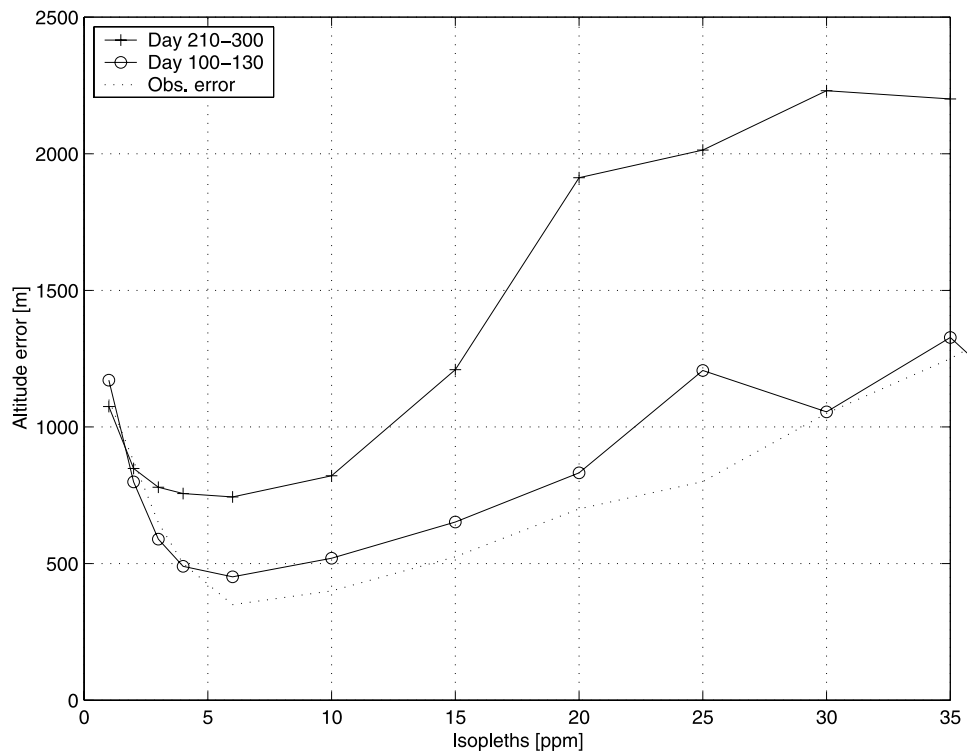


**Figure 8.** The standard deviations between the measured altitudes for the different isopleths and the polynomial fit are shown for the two time periods. The dotted line shows typical altitude errors due to thermal noise in the measurements.

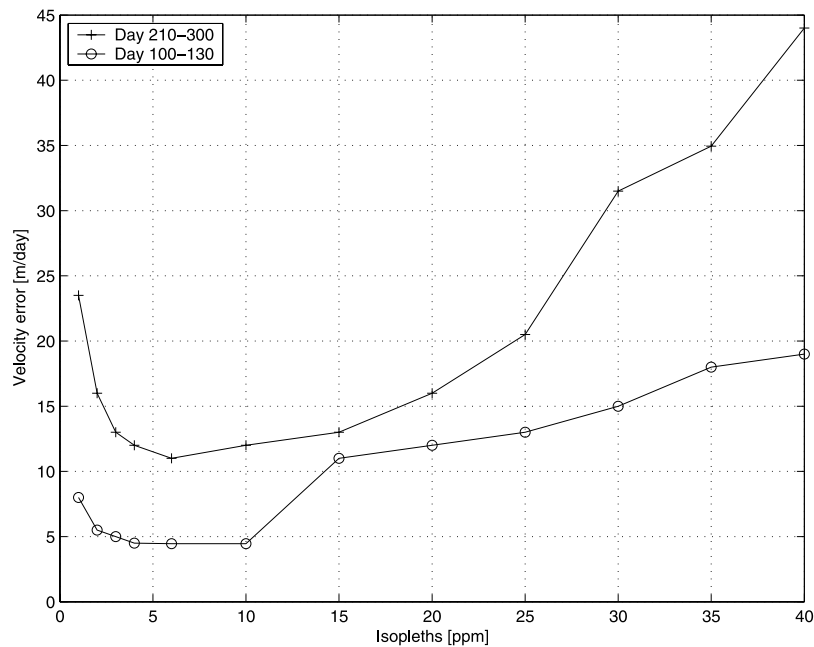


**Figure 9.** Errors in the vertical velocities are shown for the different isopleths and time periods. The large errors at isopleths 30, 35 and 40-ppm day 210–297 are explained by the few data points in these cases.

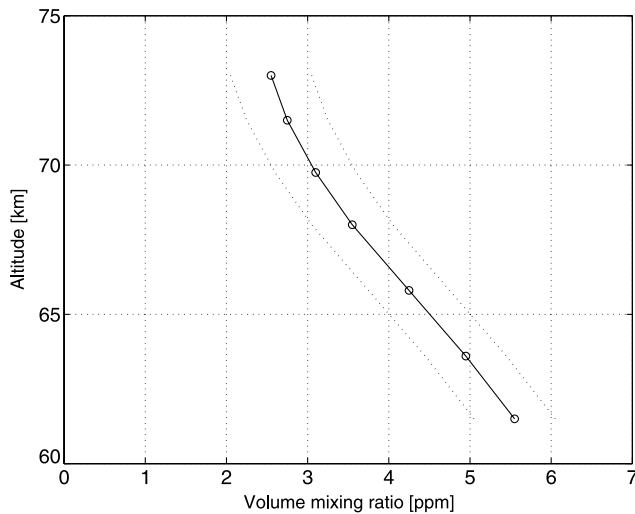


**Figure 10.** H<sub>2</sub>O profile from the middle of Mars 2002. Dots with circles show the retrieved results. The solid line shows linear interpolated values and the dashed line shows the 1 $\sigma$  error estimation from the noise in the measurements.

of the CO altitudes, and for low H<sub>2</sub>O mixing ratios, which are found in the high range of the H<sub>2</sub>O altitudes.

## 5. Influence of a Priori Information

[16] When using the optimal estimation method the a priori information describes the best guess and the believed statistics of the parameter in question. Since almost no measured profiles of mesospheric CO have been performed we use monthly zonal means of the Whole Atmosphere Community Climate Model (WACCM) [Sassi *et al.*, 2002] for the a priori information. WACCM is a General Circulation Model developed at the National Center for Atmospheric Research (NCAR) using components from three well-validated atmospheric models. The dynamics core model is based upon the NCAR Community Atmospheric Model (CAM) [Boville, 1995]; it calculates explicitly the circulation and thermodynamics of the global atmosphere from the ground to about 140 km. Chemistry and related processes are simulated using the Model for Ozone and Related chemical Tracers, MOZART [Brasseur *et al.*, 1998]. Additional chemical and physical processes needed to represent the mesosphere and thermosphere is taken from the Thermosphere, Ionosphere and Mesosphere Electrodynamics General Circulation Model (TIME-GCM) [Roble and Ridley, 1994]. A major advantage of the model for studies of the middle atmosphere is that the upper boundary is located in the lower thermosphere; this reduces the possibility of spurious reflection of planetary waves, and allows transport and chemical processes to be represented explicitly throughout the middle atmosphere. WACCM CO data has recently been compared with ground-based measurements of CO [Forkman *et al.*, 2003b]. This comparison indicate that the model can reproduce the observed seasonal cycle as well as much of its variability, although calculated column amounts are smaller than the largest values seen in the data.

[17] To diminish the influence of the a priori information in the retrieved profiles we only use data where the

measurement response >75%. We have also used a mean a priori profile for the different period of times to investigate the influence of the varying a priori profile in the retrieved profiles. The result of this investigation showed that the obtained vertical velocities are not greatly influenced by the a priori information about the vertical profile of the specie.

## 6. Results and Discussion

[18] To be able to estimate vertical velocities from the observations it is important to estimate the effects of other phenomena that affect the CO abundances like meridional flow and CO production. By analysing global and zonal WACCM model data it is clear that vertical flow explains the seasonal CO variation in the mesospheric region (50–90 km) at our latitudes in the spring and in the fall. In the summer period the vertical movements are slow and planetary wave activity affects the CO abundance in the wintertime.

[19] As seen in Figure 7 the ascending velocity between days 100–130 varies with time and altitude from about 250 m/day at 65 km altitude around day 100 to a maximum of about 450 m/day at 85–90 km altitude. In the late summer and autumn there is less variability between different altitudes and velocity. The descending velocity goes from 0 (when the downwelling starts) to a maximum of ~300 m/day at 75 km altitude day 280. The velocity errors are less or in the order of 10%. This data agrees well with Allen *et al.* [2000] although those data only cover the Antarctic stratosphere region. The vertical structure of the velocities in Figure 7 suffers from the limited vertical resolution of our observation geometry. Figure 11 shows the averaging kernels for CO at 75 and 94 km altitude and for H<sub>2</sub>O at 62 km altitude. The vertical resolution can be defined as the full width half maximum of the averaging kernel. The vertical resolution for H<sub>2</sub>O at 62 km altitude about 15 km and 25–30 km for CO at 75 and 94 km altitude. This difference in vertical resolution between CO and H<sub>2</sub>O is explained by the different broadening mechanisms that affect the two transitions.

[20] Since the pressure dominates the broadening of the H<sub>2</sub>O transition there is more altitude information in this spectrum compared to the CO spectrum where the temperature dominates the line broadening. The averaging kernels show the degree to which the retrieved volume-mixing ratio at a give height is a weight average of the real values at all heights. Since we want to monitor the vertical movement, at different altitudes, of air we want to study independent air masses. The correlation between two data points at different altitudes ( $a$ ,  $b$ ) in the obtained vertical profile,  $corr(a, b)$ , can be written as the normalized vector dot product between the averaging kernels,  $w_a$  and  $w_b$ , at the two altitudes respectively

$$corr(a, b) = \frac{w_a \cdot w_b}{\sqrt{w_a \cdot w_a} \sqrt{w_b \cdot w_b}} \quad (4)$$

By using this definition the correlation between the measured daily volume mixing ratios of CO at 75 and 94 km air is about 0.4.

[21] To compare the obtained velocities from the CO measurements with OH temperatures at 87 km we have

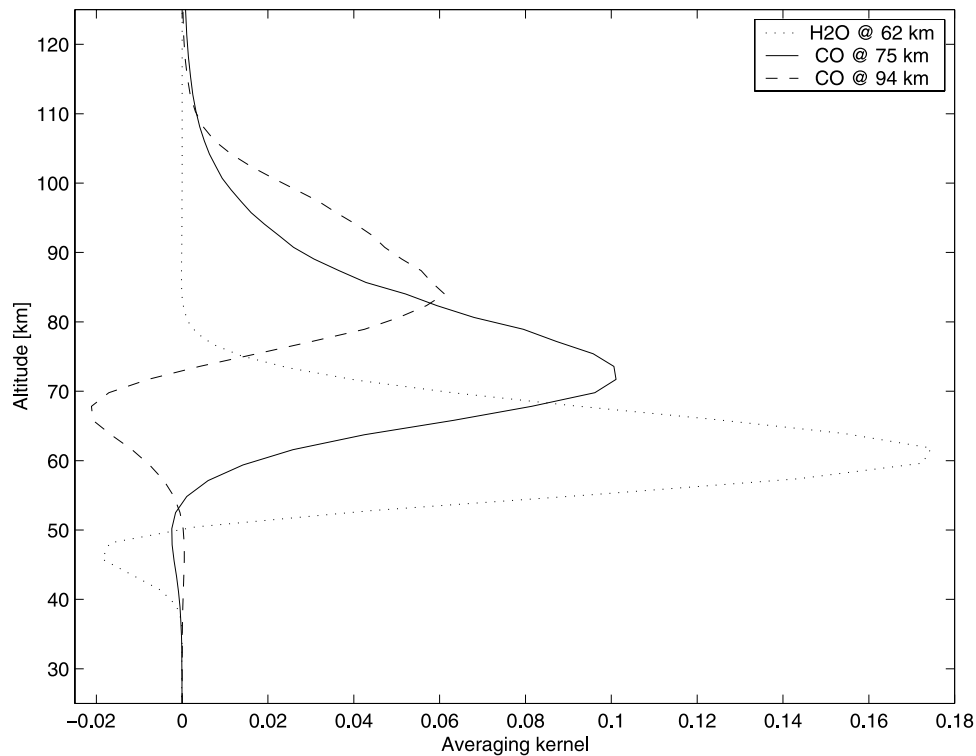


**Figure 11.** Three averaging kernels as a function of altitude from day 115. The dotted curve shows the averaging kernel from H<sub>2</sub>O data and the solid and dashed curves are averaging kernels from CO data.

studied the movement of isopleths in the pressure grid (instead of the altitude grid). When an air parcel, identified with a constant volume-mixing ratio of e.g. CO, is forced vertically up or down the pressure of the air parcel will decrease or increase depending on the direction of the movement. By monitoring the movement, in the pressure grid, of the air parcel its pressure change,  $dp$ , from day to day can be estimated. If we assume there is no heat exchange between different air parcels the first law of thermodynamics can be used to calculate the temperature change,  $dT$ , related to the pressure change,  $dp$ . The first law of thermodynamics can be written:

$$c_p \frac{dT}{dt} = \frac{1}{\rho} \frac{dp}{dt} \quad (5)$$

where the specific heat of dry air,  $c_p$ , is  $1.005 \text{ Jg}^{-1}\text{K}^{-1}$  and the density of air,  $\rho$ , is

$$\rho = \frac{p}{T \cdot R_d} \quad (6)$$

and the gas constant for dry air,  $R_d$ , is  $287.04 \text{ Jkg}^{-1}\text{K}^{-1}$ .

[22] The day-to-day relative temperature change of the air parcel can finally be written

$$\frac{dT}{T} = \frac{dp}{p} \frac{R_d}{c_p} \quad (7)$$

The day-to-day  $\frac{dT}{T}$  for the two periods of time is calculated and is shown in Figures 12 and 13. The daily relative temperature change day 130 at 0.35 Pa ( $\sim 90 \text{ km}$ ) is about

$-6 \%$  ( $-12 \text{ K/day}$ ). Day 250–280 the relative temperature change is rather constant at  $\sim 1.5 \%$  ( $3.5 \text{ K/day}$ ).

[23] These day-to-day relative changes of temperature can be compared with the OH rotational temperatures at  $\sim 90 \text{ km}$  altitude. The temperature changes estimated from the CO measurements only show the contribution from the expansion or compression of the vertically moving air. The airglow measurements show the “real” temperature including effects due to radiative processes.

[24] From the difference in the daily temperature change between the CO and airglow measurements the total net radiative heating rate, in the mesopause region ( $\sim 90 \text{ km}$ ), associated with absorption of ultraviolet radiation by ozone and molecular oxygen, and cooling by CO<sub>2</sub> at lat N  $60^\circ$  can be estimated. Figure 14 gives the daily temperature change at  $\sim 90 \text{ km}$  altitude. Day 100–130 the daily temperature change is about  $-0.5 \%$  ( $-1 \text{ K/day}$ ) and day 210–280 the daily temperature change is  $\sim 0.3\%$  ( $0.5 \text{ K/day}$ ). Combining these figures with the adiabatic temperature changes from Figures 12 and 13 the net radiative heating rates can be estimated.

[25] Day 100–130 (April–May) the daily net radiative heating rate is estimated to be about  $+11.0 \text{ K/day}$  and day 240–280 (September) the net radiative heating rate is estimated to be about  $-3.5 \text{ K/day}$ . The observation errors are about 10% and the vertical resolution is in the range 20–30 km, which means that the estimated heating rates are a mean of a 20–30 km thick altitude layer.

[26] This paper has shown that it is possible to use continuous ground-based microwave measurements of long-lived trace gases to monitor vertical movement of air in the mesosphere region. Comparison between the

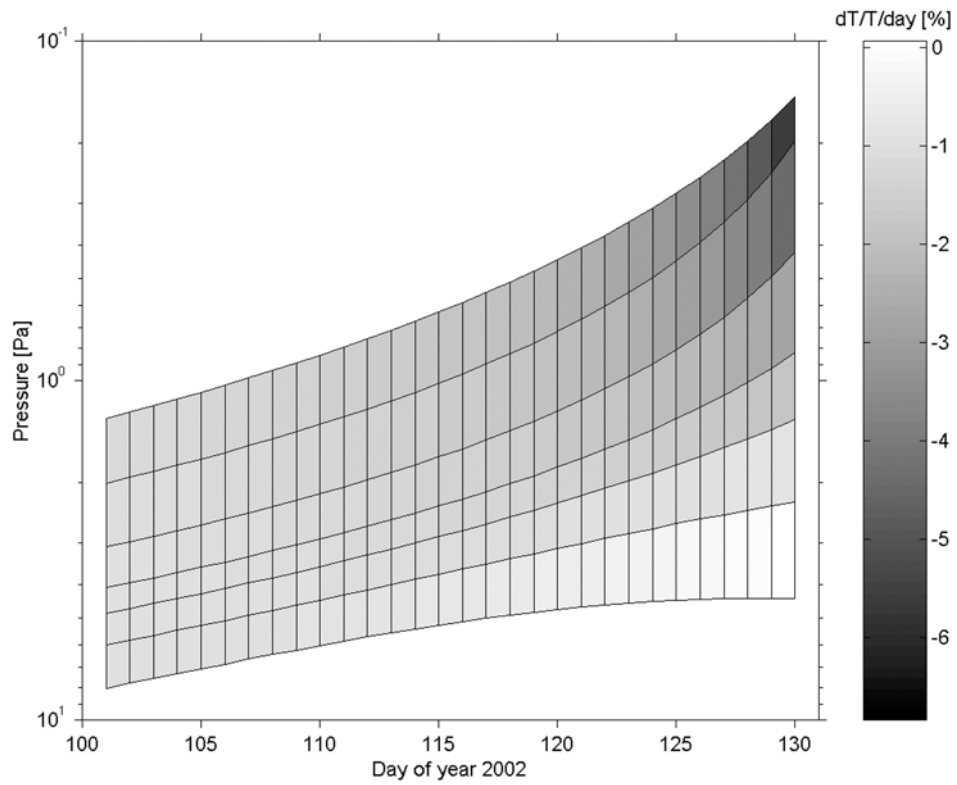


**Figure 12.** The relative temperature change as function of day and pressure in the spring as derived from the CO measurements. See color version of this figure in the HTML.

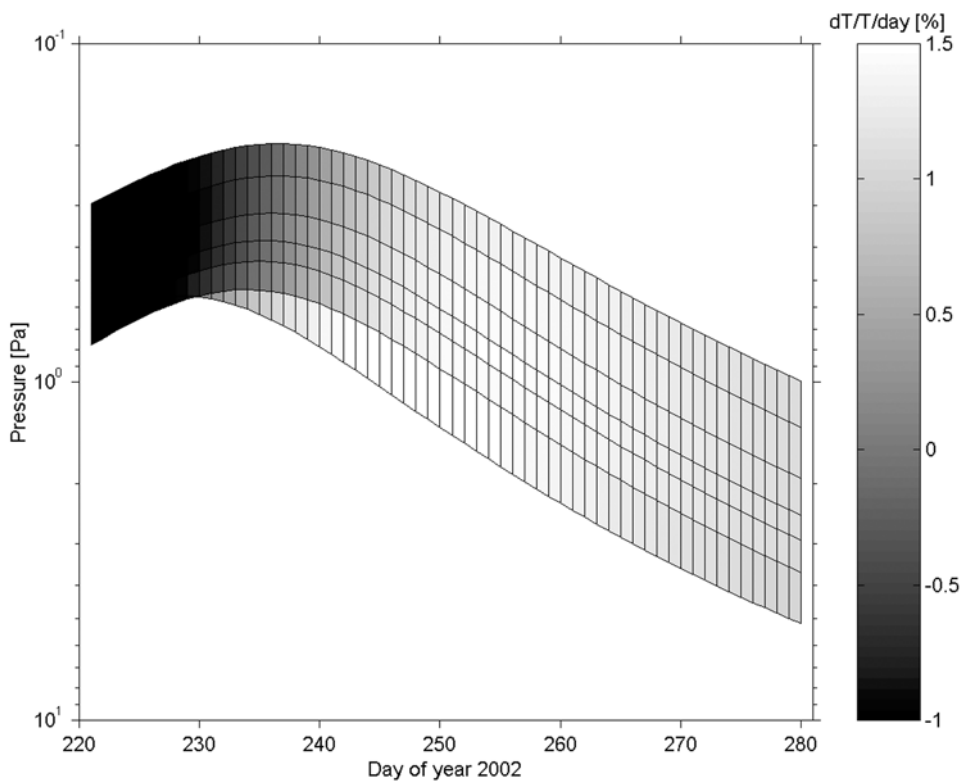


**Figure 13.** The relative temperature change as function of day and pressure in the fall as derived from the CO measurements. See color version of this figure in the HTML.

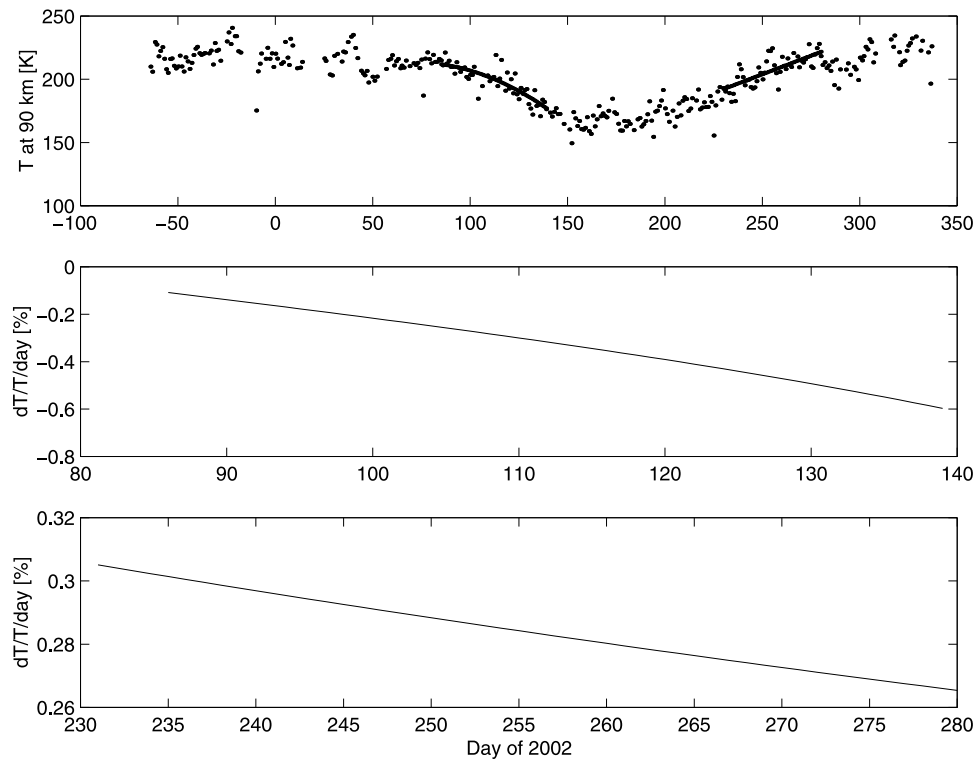


**Figure 14.** The upper plot shows the OH rotational temperature ( $\sim 90$  km) as a function of time together with polynomial fits. The middle and lower plot shows the relative day-to-day temperature change derived from the polynomial fits.

obtained vertical velocities and the mesopause temperature as estimated by the radiance of the Meinel band OH airglow gives radiative heating rates that agree well to theoretical studies.

## References

- Aellig, C. P., N. Kaempfer, and A. Hauchecorne (1995), Variability of mesospheric CO in the fall and winter as observed with ground-based microwave radiometry at 115 GHz, *J. Geophys. Res.*, *100*, 14,125–14,130.
- Allen, D. R., J. L. Stanford, N. Nakamura, M. A. Lopez-Valverde, M. López-Puertas, F. W. Taylor, and J. J. Remedios (2000), Antarctic polar descent and planetary wave activity observed in ISAMS CO from April to July 1992, *Geophys. Res. Lett.*, *27*, 665–668.
- Bevilacqua, R. M., A. A. Stark, and P. R. Schwartz (1985), The variability of carbon monoxide in the terrestrial mesosphere as determined from ground based observations of the CO  $J = 1 \rightarrow 0$  emission line, *J. Geophys. Res.*, *90*, 5777–5782.
- Boville, B. A. (1995), Middle atmosphere version of CCM2 (MACCM2): Annual cycle and interannual variability, *J. Geophys. Res.*, *100*, 9017–9039.
- Brasseur, G. P., D. A. Hauglustaine, S. Walters, P. J. Rasch, J.-F. Müller, C. Granier, and X.-X. Tie (1998), MOZART: A global chemical transport model for ozone and related chemical tracers: 1. Model description, *J. Geophys. Res.*, *103*, 28,265–28,289.
- Chandra, S., C. H. Jackman, E. L. Fleming, and J. M. Russell III (1997), The seasonal and long-term changes in mesospheric water vapor, *Geophys. Res. Lett.*, *24*(6), 639–642.
- de Zafra, R. L., and G. Muscarelli (2004), CO as an important high-altitude tracer of dynamics in the polar stratosphere and mesosphere, *J. Geophys. Res.*, *109*, D06105, doi:10.1029/2003JD004099.
- Eriksson, P. (2000), Analysis and comparison of two linear regularization methods for passive atmospheric observations, *J. Geophys. Res.*, *105*, 2927–2939.
- Espy, P. J., and J. Stegman (2002), Trends and variability of mesospheric temperatures at high-latitudes, *Phys. Chem. Earth, Parts A/B/C*, *27*(6–8), 543–553.
- Espy, P. J., W. R. Pendleton Jr., G. G. Sivjee, and M. P. Fetrow (1987), Vibrational development of the  $N_2^+$  Meinel band system in the aurora, *J. Geophys. Res.*, *92*, 11,257–11,261.
- Forkman, P. (2003), Ground based measurements of upper atmospheric CO and H<sub>2</sub>O using microwave radiometry, *Tech. Rep. 456*, Sch. of Elect. Eng., Chalmers Univ. of Technol., Onsala, Sweden.
- Forkman, P., P. Eriksson, and A. Winnberg (2003a), The 22 GHz radio-astronomy receiver at Onsala Space Observatory, *J. Quant. Spectrosc. Radiat. Transfer*, *77*, 23–42.
- Forkman, P., P. Eriksson, A. Winnberg, R. R. Garcia, and D. Kinnison (2003b), Longest continuous ground-based measurements of mesospheric CO, *Geophys. Res. Lett.*, *30*(10), 1532, doi:10.1029/2003GL016931.
- Garcia, R. R., F. Stordal, S. Solomon, and J. T. Kiehl (1992), A new numerical model of the middle atmosphere: 1. Dynamics and transport of tropospheric source gases, *J. Geophys. Res.*, *97*, 12,967–12,991.
- López-Puertas, M., M. A. López-Valverde, R. R. Garcia, and R. G. Roble (2000), A review of CO<sub>2</sub> and CO abundances in the middle atmosphere, in *Atmospheric Science Across the Stratopause*, *Geophys. Monogr. Ser.*, vol. 123, pp. 83–100, AGU, Washington, D. C.
- Nedoluha, G. E., R. M. Bevilacqua, R. M. Gomez, W. B. Waltman, B. C. Hicks, D. L. Thacker, and W. A. Matthews (1996), Measurements of water vapor in the middle atmosphere and implications for mesospheric transport, *J. Geophys. Res.*, *101*, 21,183–21,194.
- Roble, R. G., and E. C. Ridley (1994), A thermosphere-ionosphere-mesosphere-electrodynamics general circulation model (TIME-GCM): Equinox solar cycle minimum simulations (30–500 km), *Geophys. Res. Lett.*, *21*, 417–420.
- Sassi, F., R. R. Garcia, B. A. Boville, and H. Liu (2002), On temperature inversions and the mesospheric surf zone, *J. Geophys. Res.*, *107*(D19), 4380, doi:10.1029/2001JD001525.
- Seele, C., and P. Hartogh (1999), Water vapor of the polar middle atmosphere: Annual variation and summer mesosphere conditions as observed by ground-based microwave spectroscopy, *Geophys. Res. Lett.*, *26*, 1517–1520.

P. Eriksson, P. Forkman, and D. Murtagh, Onsala Space Observatory, Department of Radio and Space Science, Chalmers University of Technology, S-43992 Onsala, Sweden. (forkman@oso.chalmers.se)  
P. Espy, British Antarctic Survey, Cambridge CB3 0ET, UK.